공학석사학위논문

케이블 구동식 평면 소프트 액추에이터의 형상 설계

Configuration Design of Planar Cable-Driven Soft Actuators

2021년 2월

서울대학교 대학원

기계공학부

신 승 호

케이블 구동식 평면 소프트 액추에이터의 형상 설계

Configuration Design of Planar Cable-Driven Soft Actuators

지도교수 김 윤 영

이 논문을 공학석사 학위논문으로 제출함

2020년 10월

서울대학교 대학원
기계공학부
신 승 호

신승호의 공학석사 학위논문을 인준함

2020년 12월

위 원 장 _____ (인)

부위원장 _____ (인)

위 원 _____ (인)

Abstract

Soft robots have recently attracted considerable attention thanks to their unparalleled advantages over traditional rigid robots in terms of adaptability and stability. However, due to the accompanying complexity, their usability is not up to expectations. In particular, the design of soft robots to date has required a lot of experience and time. In this study, the configuration of a planar cable-driven soft actuator is designed in a systematical fashion. To this end, the continuously varying curvature of the soft actuator is simply expressed using Legendre polynomials. This expression minimizes the number of parameters needed for the design formulation while preserving their physical meanings. In addition, these parameters are suitable for drawing maps that visualize their dependency on each other. The maps allow us to see if there are feasible answers before we start the design process. The procedure of optimization-based design proposed in this thesis is validated with arbitrarily chosen target values. Experimental results show that this procedure works well in reality as well.

Keyword: optimization-based design, cable-driven actuators, soft robots, design feasibility

Student Number: 2018-24324

Contents

List of Tables

List of Figures

Chapter 1. Introduction

Soft robots are systems that are made of materials such as rubber and silicone, which have similar stiffness to biological tissue, and can autonomously perform mechanical functions [1]. These materials make the performance of soft robots completely different from that of traditional, rigid robots. While traditional robots are expected to perform an assigned task quickly and accurately, soft robots are expected to handle diverse, instant interactions in an unstructured environment. This adaptability comes from the fundamental properties of soft materials that conform to surrounding surfaces by deforming themselves into continuous morphology [2]. This is why soft robots are studied for use in exploration of unpredictable terrain, e.g. disaster sites and military areas.

The adaptability also enables safe contact between the system and humans. In the event of a collision, increased contact time reduces impact force and much of the energy from the collision is converted into deformation of the materials. The safe interaction between soft robots and humans provides the possibility of use for human assistance or medical applications [3]. Soft robots can also construct wearable devices because they have similar elasticity to human skin or muscles.

Despite these outstanding potentialities, the usability of soft robots in various

fields is still at the laboratory level. It is due to the difficulties inherent in the systematic design of soft robots. Establishing a general design routine has been hindered by their tricky features—large deformation, nonlinear behavior of materials, and sensitivity to the environment [4]. A common practice so far is to mimic living creatures [5]-[7] or perform a number of trials and errors mainly guided by engineers' intuition [8]. These methods consist of designing a plausible prototype first, and then finding and reflecting improvements. Usually this process is repeated until the desired performance is achieved, requiring a considerable amount of labor and time. The results produced in this way are likely to be familiar to the researchers rather than optimal. Furthermore, if new design goals are given, the process should be carried out from scratch.

If a systematic design method that does not require human creativity or arduous repetition is available, the design of soft robots can be greatly facilitated. Motivated by this need, recent studies have sought to present optimization-based design methods. One of the most striking examples is the automatic design of amorphous soft robots, which optimizes their three-dimensional shape only based on given target performance without any geometric parameters [9]. It can fully exploit the unconstrained design space, but subsequent studies are still needed with respect to the actual fabrication and actuation. A more realistic example is the non-

parametric design of pneumatic soft actuators, where a chamber structure and material distribution are optimized so that the actuator deforms as desired [10].

Since the above two examples do not require design parameters, human intuition is completely excluded and the design process is carried out thoroughly in a computational manner. This is an advantageous strategy in that it reserves all the potential designs, but it involves complex formulation and high computational costs. For handier design automation, design parameters are usually introduced. The parametric designs have been applied to generate target deformation of fiber-reinforced [11], [12] or multi-material [13] pneumatic soft actuators.

Unlike those studies, this thesis investigates design of cable-driven soft actuators. The advantage of using cable transmission is that the driving units, usually electric motors, can be installed outside the actuator and the transmission is immediate, enabling miniaturization and agile actuation [14]. In addition, electric motors are cheaper, more reliable, and easier to control than their counterparts [15]. In this thesis, an optimization-based design process is proposed to identify the desired cable routing of a planar cable-driven soft actuator. Its end-effector and body shape are induced to fit a given target without any advanced sensing or control.

The effect of cable routing on performance of the actuators has been

addressed in a couple of studies. In [16], the merits of spiral routings over straight routings are analyzed focusing on workspace and robot motions. Strictly speaking, the actuator presented in the paper is not a soft robot, but a continuum robot since it is a flexible backbone instead of a soft body that supports its weight. Along the backbone several support disks are attached to it at equal intervals and the disks have several holes. Cables pass one hole for each disk, so a different combination of the hole selection creates different cable routings. Next, in [17], a cable routing of a planar cable-driven soft actuator is optimized to improve its workspace and manipulability. The cable routing is determined by binary hole selection. Finally, in [18], a multi-legged soft robot is designed, each leg of which is a cable-driven soft actuator. The resulting cable routing improves stiffness of each actuator and thus gait efficiency of the entire robot.

Most studies on cable routing to date, including the three above, deal with discrete routing of the cables. In these cases, the cable routing is determined as a combination of the selection from a finite number of holes. On the other hand, continuous cable routing is considered in this study, which generates more diverse and delicate actuation and allows for fine-tuning of the actuation. The continuous cable routing is realized by forming a thin curved channel inside the silicone body and passing a cable through it. Hence, to fabricate the continuous cable routing, the

actuator body should be made almost completely of soft materials rather than supported by flexible, slender backbones. Fully soft actuators can have continuous cable routings, but are not appropriate to conveying large forces due to the low stiffness. This makes the actuators better suited for the last one inch of direct interaction with other systems than for performing a structural function. Also, the softness aggravates difficulty in predicting the actuated shape because of mechanical dependency between the parts. This complexity highlights again the need for optimization-based design.

In chapter 2, this thesis first gives an overview of the actuators to be designed, and delineates how they are modeled to simulate the actuation. In chapter 3, deformation of the actuators is represented by a novel expression to define the objective function of the optimization problem. This problem may not have an appropriate solution, so a kind of guide map is presented in Chapter 4 to determine the feasibility in advance. The proposed design procedure is validated in Chapter 5 by fabricating actual specimens and experimenting with them. Lastly, Chapter 6 recapitulates the entire design process and concludes the thesis, discussing its efficacy and potential.

Chapter 2. Modeling

A brief illustration of the actuators designed in this study is shown in Fig. 2.1. The cylindrical silicone body is made of a material that has adequate stiffness, allowing sufficient actuation with small tension. One side of the silicone body is fixed to the underside of a flat base. In the silicone body is a continuously curved channel, through which a cable is threaded. The distal end of the cable is knotted, preventing it from escaping the channel. It drives the actuator by transmitting tension applied at its proximal end to all contact surfaces: the inner surface of the channel and the point pressed by the knot. The transmitted tension deforms the silicone body into a certain configuration, which is determined by the cable routing. For a detailed fabrication process and an experimental setup, refer to Chapter 5.

2.1. Coupled Cosserat Model

Deformation of the actuators is modeled by the coupled Cosserat model [19]. This model is composed of two simpler models: one is a classical Cosserat rod model and the other is its cable version. The coupled model yields a system of nonlinear differential equations in explicit form. The subsequent paragraphs briefly skim

through the derivation of the equation. Readers may refer to [19] for details.

The Cosserat rod model starts by approximating a slender rod, which corresponds to the silicone body of this study, in one dimension and defining local frames at each point of the rod with a length parameter $s \in [0, L]$, where L is the length of the rod. Each local frame has its x-axis tangential to the centerline of the rod and z-axis normal to the plane including the channel. Location and orientation of each local frame with respect to the global frame, the one at the fixation point on the base, are defined as a vector $\mathbf{p}(s) \in \mathbb{R}^3$ and a matrix $R(s) \in SO(3)$, respectively, as described in Fig. 2.2 (a). Linear and angular changes of the local frames along s are expressed as follows:

$$\begin{aligned} \dot{\mathbf{p}} &= R\mathbf{v} \\ \dot{R} &= R\hat{\mathbf{u}}, \end{aligned} \tag{2.1}$$

where $\mathbf{v}(s)$ and $\mathbf{u}(s)$ represent the linear and the angular *spatial* velocity with respect to s expressed in global coordinates. Given internal forces $\mathbf{n}(s)$ and moments $\mathbf{m}(s)$ and external distributed forces $\mathbf{f}(s)$ and moments $\mathbf{l}(s)$ as shown in Fig. 2.2 (b), we have static equilibrium equations:

$$\begin{aligned} \dot{\mathbf{n}} + \mathbf{f} &= \mathbf{0} \\ \dot{\mathbf{m}} + \dot{\mathbf{p}} \times \mathbf{n} + \mathbf{l} &= \mathbf{0}, \end{aligned} \tag{2.2}$$

which are expressed in local coordinates. With two stiffness matrices

$$\begin{aligned} K_{se} &= \mathrm{diag}(EA, GA, GA) \\ K_{bt} &= \mathrm{diag}(GJ, EI, EI), \end{aligned} \tag{2.3}$$

linear constitutive equations can be obtained as

$$\begin{aligned} \mathbf{n} &= RK_{se}(\mathbf{v} - \mathbf{v}^*) \\ \mathbf{m} &= RK_{bt}(\mathbf{u} - \mathbf{u}^*). \end{aligned} \tag{2.4}$$

Finally, boundary conditions

$$\mathbf{p}(0) = \mathbf{p}_0, \quad R(0) = R_0, \quad \mathbf{n}(L) = \mathbf{F}_L, \quad \mathbf{m}(L) = \mathbf{M}_L \tag{2.5}$$

complete the Cosserat rod model.

We can model the whole actuator by considering a portion of the external forces and moments acting on the rod as those from the cable:

$$\begin{aligned} \mathbf{f} &= \mathbf{f}_e + \mathbf{f}_c \\ \mathbf{l} &= \mathbf{l}_e + \mathbf{l}_c. \end{aligned} \tag{2.6}$$

To express $\mathbf{f}_c(s)$ and $\mathbf{l}_c(s)$ in terms of $\mathbf{p}(s)$ and $R(s)$, the cable routing $\mathbf{r}_c(s) = \begin{bmatrix} 0 & y_c(s) & z_c(s) \end{bmatrix}^T$ is defined as coordinates of the cable on a section of the silicone body as described in Fig. 2.3 (a). Note that $z_c = 0$ for all s because only planar cable routings are covered in this study and $|y_c|$ must be less than the actuator radius r. Then, the cable routing with respect to the global frame is expressed as

$$\mathbf{p}_c = \mathbf{p} + R\mathbf{r}_c. \tag{2.7}$$

Since ideal cables carry no internal moments and neglecting friction makes internal forces on cable sections dependent only on the applied tension τ, we have

$$\begin{aligned} \mathbf{n}_c &= \tau \frac{R^T \dot{\mathbf{p}}_c}{\|\dot{\mathbf{p}}_c\|} \\ \mathbf{m}_c &= \mathbf{0}. \end{aligned} \tag{2.8}$$

Referring to Fig. 2.3 (b), the forces and moments exerted to the silicone body by the cable can be obtained as follows:

$$\begin{aligned} \mathbf{f}_c &= \dot{\mathbf{n}}_c \\ \mathbf{l}_c &= \mathbf{r}_c \times \mathbf{f}_c. \end{aligned} \tag{2.9}$$

By inserting (2.9) into (2.6) and putting the equations (2.1)-(2.6) together, one can get the governing equation in the form of

$$\dot{\mathbf{y}} = f(\mathbf{y}), \tag{2.10}$$

where $\mathbf{y}$, a state variable, contains the values of $\mathbf{p}$, R, $\mathbf{v}$, and $\mathbf{u}$.

From the derivation so far, we can identify several important properties of the coupled Cosserat model. First, since the model introduces local coordinate systems, geometric nonlinearity is reflected and thus it can deal with large deformation of the actuator. In addition, it is compatible with general external loads by taking into account not only the point forces/moments but also the distributed forces/moments, unlike some models adopted by prior researches. This nonlinearity and generality is appropriate for mechanical analysis of cable-driven soft actuators. The model

also includes some simplifications for efficiency of the analysis. Basically the model is one-dimensional, so the slenderer the silicone body is, the more accurate the model is. The diagonal stiffness matrices in the equation (2.3) assume linearity and independence of axial, shear, bending, and torsional deformation, which is the case when the strain is small enough. Finally, sectional deformation, channel width, and friction are ignored. The resulting equation (2.10) is in explicit form that can be solved with any kind of numerical solvers. In this thesis, a built-in function *ode45* of MATLAB software was used. One static analysis took about 0.05s with Intel Core i7-6700 CPU.

2.2. Cable Routing

The curve of the channel is constructed by a B-spline with five control points as depicted in Fig. 2.4 (a). The control points are equally spaced along s and y-coordinates of the points in the local frame are to be designed. The number of control points was determined to be large enough to represent a variety of curves, but not excessive. Too many control points may make the curve too tortuous, which results in too complex deformation of the silicon body. This raises concerns about accuracy and speed of the analysis, but above all, it is difficult to fabricate and realize such twisted channels. The five control points are given as

(s_0, y_0), (s_1, y_1), $\cdots$, (s_4, y_4) and the degree of the curve is set to $p = 3$. Then, basis functions of the B-spline are inductively defined as

$$\begin{aligned} N_{i,0}(\zeta) &= \begin{cases} 1, & \text{if } \zeta_i \le \zeta < \zeta_{i+1} \text{ and } \zeta_i < \zeta_{i+1} \\ 0, & \text{otherwise} \end{cases} \\ N_{i,j}(\zeta) &= \frac{\zeta - \zeta_i}{\zeta_{i+j} - \zeta_i} N_{i,j-1}(\zeta) + \frac{\zeta_{i+j+1} - \zeta}{\zeta_{i+j+1} - \zeta_{i+1}} N_{i+1,j-1}(\zeta), \end{aligned} \tag{2.11}$$

where $\zeta \in [0,1]$ and the knots are set as $\zeta_0 = \zeta_1 = \zeta_2 = \zeta_3 = 0$, $\zeta_4 = 0.5$, and $\zeta_5 = \zeta_6 = \zeta_7 = \zeta_8 = 1$. Finally, the B-spline is defined by

$$\begin{bmatrix} s(\zeta) \\ y_c(\zeta) \end{bmatrix} = \sum_{i=0}^{4} \begin{bmatrix} s_i \\ y_i \end{bmatrix} N_{i,p}(\zeta). \tag{2.12}$$

Since $\mathbf{r}_c(s)$ involves y_c as a function of the length parameter s, not of ζ, and the equation (2.10) requires the first and the second derivatives of $\mathbf{r}_c(s)$, some helpful tricks are used:

$$\begin{aligned} \frac{dy_c}{ds} &= \frac{dy_c}{d\zeta} \cdot \left(\frac{ds}{d\zeta} \right)^{-1} \\ \frac{d^2 y_c}{ds^2} &= \frac{d^2 y_c}{d\zeta^2} \cdot \left(\frac{ds}{d\zeta} \right)^{-2} - \frac{dy_c}{d\zeta} \cdot \frac{d^2 s}{d\zeta^2} \cdot \left(\frac{ds}{d\zeta} \right)^{-3}. \end{aligned} \tag{2.13}$$

One of the useful properties of B-splines is that the generated curve is contained inside convex hulls that consist of the lines connecting control points. This property guarantees viability of the design because the channel must not leave the silicone body.

2.3. Material Properties

In general, mechanical properties of rubber-like materials should be carefully defined and measured. This is because it is unclear whether the moduli obtained from standard experiments fit well under other conditions such as various shapes, sizes, and loads. Furthermore, the properties vary depending on temperature, humidity, fabrication processes, and the time elapsed since fabrication. Thus, some studies have either devised new experiments to measure moduli that are just right for their research situations [20], or used FEM simulations to determine the moduli [11], rather than simply adopting known literature values. In this thesis, the mechanical moduli are determined by comparing results from MATLAB simulations and experiments. To this end, three basic cable routings described in Fig. 2.4 (b)-(d) were first chosen. Then, both simulations and experiments are conducted with tension increasing from zero to a prescribed maximum in eight steps. For a detailed experimental setup, refer to Chapter 5. At each step and the rest state, coordinates and orientation of the end-effector (x_0, y_0, θ_0), (x_1, y_1, θ_1), $\cdots$, (x_8, y_8, θ_8) are obtained. The discrepancy between values from the simulations and the experiments, i.e.,

$$\sum_{i=0}^{8}\left[(x_{i,s}-x_{i,e})^2+(y_{i,s}-y_{i,e})^2+(\theta_{i,s}-\theta_{i,e})^2\right] \tag{2.14}$$

is minimized by fitting EA, GA, and EI of the stiffness matrices in the equation (2.3). Note that each of the three rigidities is treated as a single variable and GJ is not included because the planar actuator of interest is free from torsion. The minimization problem was solved with a built-in function *fsolve* of MATLAB. The fitted moduli are listed in Table 2.1 and the simulations using them are compared to experimental results in Fig. 2.5 and 2.6.

Table 2.1. Fitted material moduli for mechanical properties

Axial Rigidity *EA*	**Shear Rigidity** *GA*	**Bending Rigidity** *EI*
26.6964N	1.70866N	115.117N·mm^2

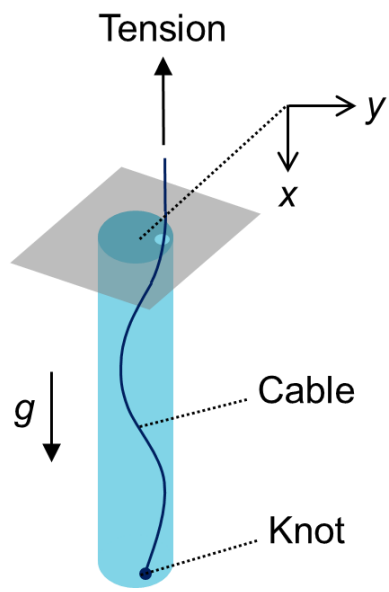

Fig. 2.1. An illustration of the cable-driven planar soft actuator to be designed. The cylindrical silicone body is attached vertically to the base and has a curved channel in it. The cable runs through the channel and the tension applied to the cable causes deformation of the actuator.

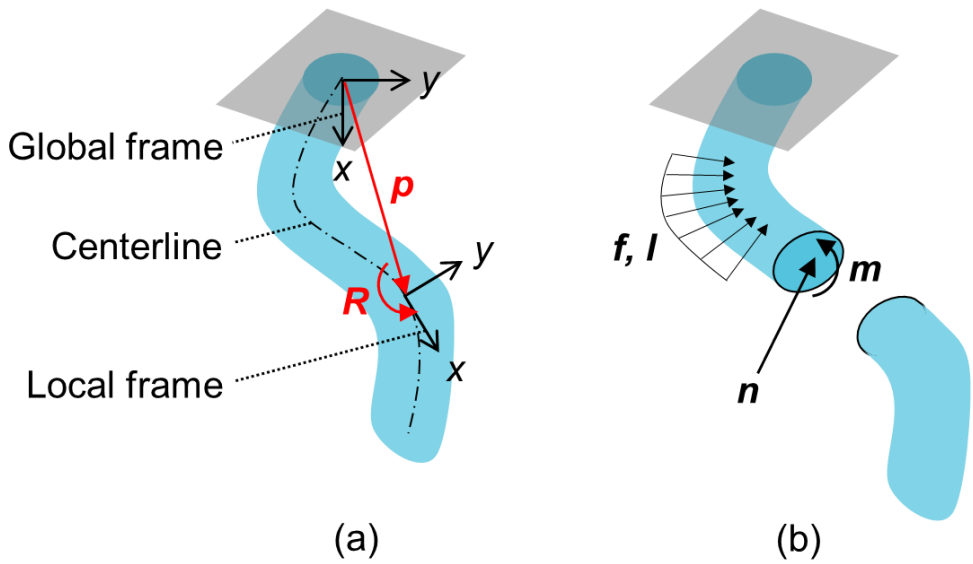

Fig. 2.2. (a) Location **p** and orientation R of local frames with respect to the global frame. (b) External and internal loads exerted to the silicone body.

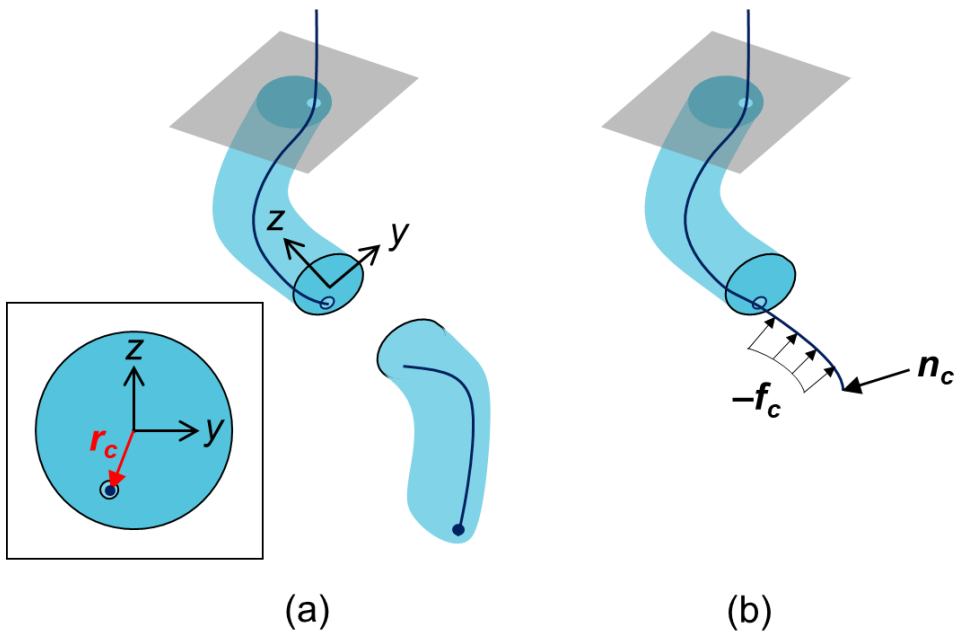

Fig. 2.3. (a) A cable routing $\mathbf{r}_c$ defined as coordinates of the cable on a section of the silicone body. (b) External and internal forces exerted to the cable. There is a negative sign because $\mathbf{f}_c$ is defined as a force that the cable exerts to the silicone body. The force that the cable exerts on the channel surface can be replaced by external forces and moments acting on a centerline of the silicone body.

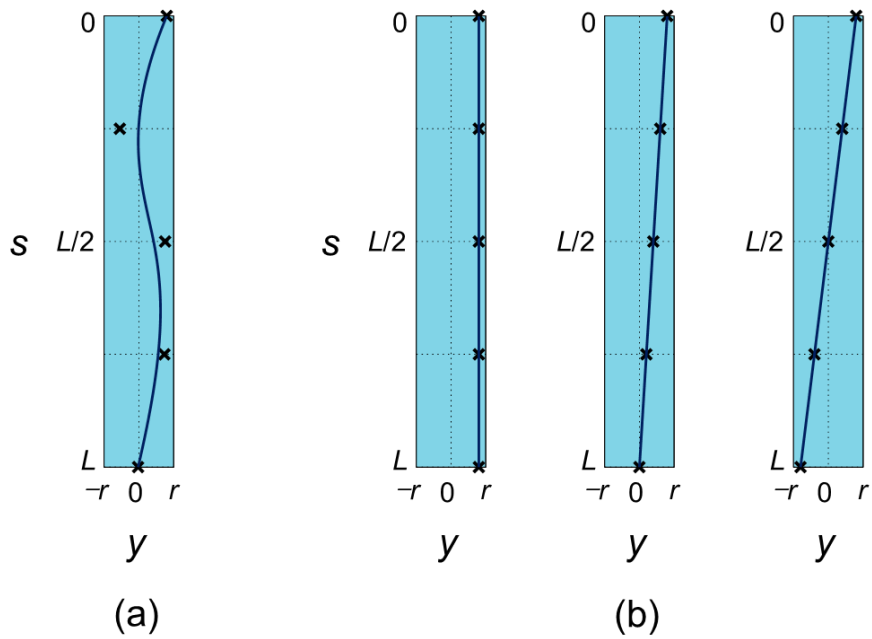

Fig. 2.4. (a) A cable routing constructed as a third-order B-spline with five control points. The control points, the black crosses, are equally spaced in s-axis and y-coordinates of the points are to be designed. (b) Three basic cable routings chosen for modulus fitting. Simulations and experiments are performed with those routings, and the results are compared to find the fittest material moduli.

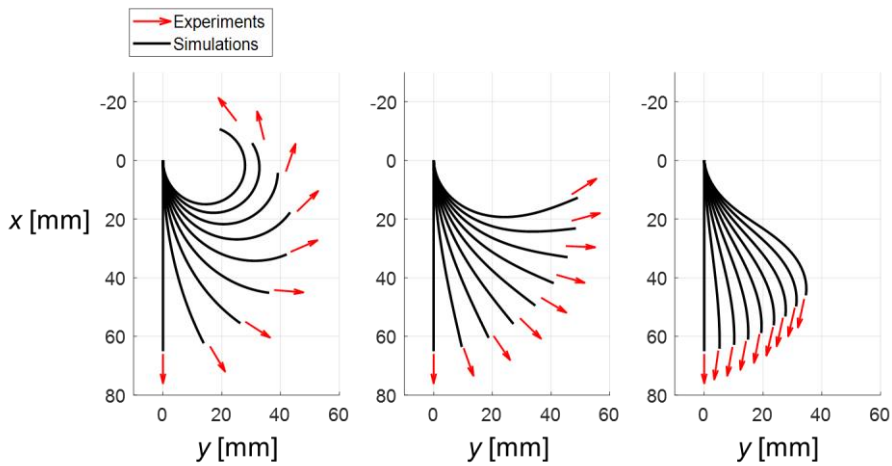

Fig. 2.5. Comparison between the simulations using the fitted moduli and the experimental results. The three basic cable routings in Fig. 2.4 (b) were used. Each black curve represents the silicone body. The red arrows represent orientation of the end-effector and their tails are located at the end-effector.

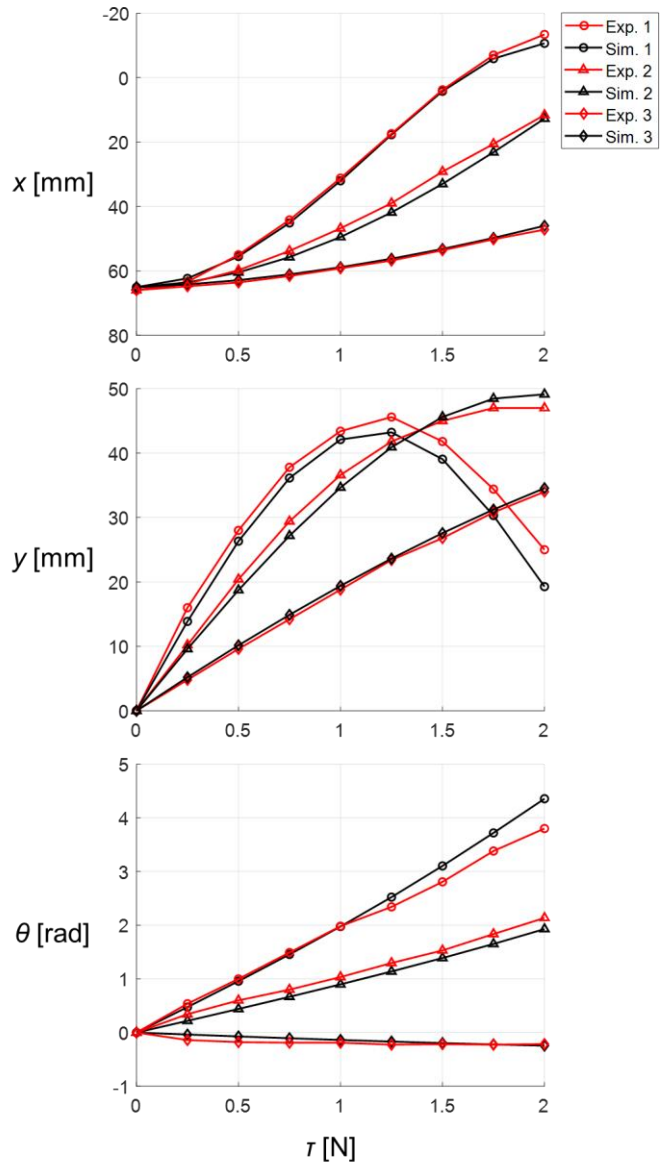

Fig. 2.6. Coordinates and angles of the end-effector in Fig. 2.5.

Chapter 3. Configuration Expression

Optimization-based design is accomplished by minimizing the difference between performance of a proposed design and target values. The difference, an objective function of the optimization problem, is defined by quantifying the performance and comparing the quantities. The definition must be made with great care because it determines the quality of the results. In particular, since this study takes the overall configuration of the silicone body as the performance, a proper expression of the configuration is required. In the following few sections, Legendre polynomials are introduced to efficiently express the configuration and define the objective function.

3.1. Expressive Degrees of Freedom

Configurations of soft actuators intrinsically have infinite degrees of freedom as described in Fig. 3.1. However, only some finite number of degrees of freedom can be considered because simulation and optimization are both performed numerically. Among the entire infinite degrees of freedom, let's call ones that are used directly in design *expressive* degrees of freedom.

The simplest expression of the configurations presented in preceding studies

uses two expressive degrees of freedom: constant curvature and an arc length [21]. This expression is usually used when it can be assumed that the actuator has the shape of a single arc, curvature of which is constant. The assumption of constant curvature, one of the earliest attempts to describe continuum deformation, cannot address distributed loads such as gravity, which is common in the real environment. This expression has been usually applied to pneumatic actuators or continuum (not soft) robots, which either do not show acute local changes of curvature, or have bulky, stable bases. These actuators obviate the need to consider initial angles at fixation point on the base. However, cable-driven soft actuators may have a fairly large initial angle and therefore require an additional degree of freedom to express it.

Approximating soft actuators to several consecutive arcs, instead of just one arc, can greatly improve accuracy of the expression. The assumption of piecewise constant curvature was devised to overcome the limits of the single arc assumption. This advanced expression works well when the actuator has different curvature for several different sections, as is the case in [22] and [23]. However, it fails to describe curvature that varies continuously. The continuous variation in curvature, a common feature of cable-driven soft actuators, makes it rely on heuristic ways to decide the number of arcs into which the actuator is split. Moreover, searching for

the fittest dimensions of the arcs involves an extra optimization problem.

If only position of the actuator's end-effector is important and its overall silhouette is not concerned for design, there is an alternative option: expressing the configuration with just end-effector coordinates. According to this expression, two expressive degrees of freedom are necessary for planar actuators and three for spatial ones. Although it gives up representing the body shape, it is still worth consideration since the position of end-effectors is the most crucial for many applications. If needed, position of midpoints may be taken as additional expressive degrees of freedom.

Increasing the number of expressive degrees of freedom enables clearer revelation of the configuration. At the same time, though, it entails increased computational costs. This raises the question of compromise between efficiency and accuracy. In addition, if excessive degrees of freedom are used, it is not possible to affirm that the combination of target values given for each degree of freedom is feasible, or even reasonable. This is because the degrees of freedom are not independent like those of rigid mechanisms. Especially, for cable-driven soft actuators, the dependency between their parts is extreme as all the parts are simultaneously deformed by a single input of tension. Even if the combination of target values is sure to be feasible, stricter requirements from superfluous

expressive degrees of freedom, along with the curse of dimensionality, give rise to a smaller solution space, making the optimization-based design less promising. In conclusion, for successful design, the key is to keep the expressive degrees of freedom fewest as long as they express the configurations clearly enough. Also, it is better to use expressive degrees of freedom that give us a rough indication of how they depend on each other.

3.2. Legendre Polynomial Expression

In this study, the constant curvature assumption introduced above is extended to higher orders using Legendre polynomials. In this way, a novel expression for the configurations of soft actuators are derived. In the original assumption of constant curvature, the curvature is assumed to be a constant—a zeroth-order polynomial:

$$\kappa(s) = a_0. \tag{3.1}$$

Alternatively, the curvature can be set as a higher-order polynomial using Legendre polynomials to represent varying curvature as follows:

$$\kappa\big(s(t)\big) = \hat{\kappa}(t) = a_0 P_0(t) + a_1 P_1(t) + a_2 P_2(t) + \cdots, \tag{3.2}$$

where $t = (2s - L)/L$ is a normalized parameter in $[-1,1]$ and P_i is an i th-order Legendre polynomial. To list a few Legendre polynomials from the lower order, there are

$$P_0 = 1, \quad P_1 = t, \quad P_2 = \frac{1}{2}(3t^2 - 1), \quad \cdots. \tag{3.3}$$

Now an appropriate order is selected and coefficients of the terms below that order are taken as expressive degrees of freedom. With these degrees of freedom, a configuration of the silicone body is approximated to a more complex shape than an arc, which can be seen from Fig. 3.2.

However, they only represent an overall shape of the silicone body and do not indicate an angle to which the actuator is positioned with respect to the base. It is essential to introduce an additional expressive degree of freedom to determine the angle because the initial angle is not negligible for cable-driven soft actuators in general, as mentioned earlier. However, rather than the initial angle θ_0, the end-effector coordinates (x_e, y_e) are taken as the additional expressive degrees of freedom, as they also can represent the initial angle and are of more interest than the initial angle itself. Directly expressing the end-effector coordinates eliminates their inaccuracy resulting from unconsidered higher-order terms of the curvature. To sum up, for example, if we are to approximate the curvature as a first-order polynomial, we have four expressive degrees of freedom: (x_e, y_e, a_0, a_1). With the same number of expressive degrees of freedom, one can approximate the silicone body to two consecutive arcs assuming that the initial angle is small enough.

The proposed expression of a configuration using Legendre polynomials has several remarkable advantages. First, the order of the approximated polynomial can be easily increased in an additive way, since all P_i's are orthogonal to each other. In other words, if we want to increase the order to which the curvature is approximated from n to $n+1$, the only coefficient to be computed is that of $(n+1)$ th-order term since all the other coefficients are still valid. This orthogonality also allows the coefficient a_0 to retain its physical meaning—the mean curvature. It is proved by the following properties of Legendre polynomials:

$$\int_{-1}^{1} P_i dt = 0, \qquad i \geq 1, \tag{3.4}$$

and, thus,

$$\frac{1}{L}\int_0^L \kappa ds = \frac{1}{2}\int_{-1}^{1} \hat{\kappa} dt = a_0. \tag{3.5}$$

On the other hand, usual polynomial regression analysis requires all coefficients to be obtained again whenever the order of regression changes. This makes it difficult for the coefficients to have a physical meaning.

The proposed expression is highly advantageous if the curvature of the actuator varies continuously, which is often the case for cable-driven soft actuators. If the assumption of piecewise constant curvature is applied to these actuators, we have to split them into many short pieces, which greatly increases the number of

expressive degrees of freedom. However, by including higher-order terms to the approximated curvature polynomial, we can reduce or even keep as one the required number of pieces. The small number of expressive degrees of freedom also makes it relatively simpler to visualize their interdependency, which is discussed in detail in Chapter 4.

3.3. Numerical Issues

Simulations give us coordinates of the points that make up the curve of silicone body. Then, the curvature is calculated by differentiating twice the coordinates. In practice, numerically computing the second derivatives poses some numerical issues. Thus, in this thesis, integral of the curvature is used instead of the curvature itself. With the initial angle θ_0, we have

$$\theta(s) = \int_0^s \kappa ds + \theta_0, \tag{3.6}$$

where $\theta(s)$ represents the angle between a tangent at s and a line normal to the base. Since Legendre polynomials have useful integral properties such that

$$\begin{aligned} &\int P_0 dt = P_1 + C \\ &\int P_i dt = \frac{1}{2i+1}(P_{i+1} - P_{i-1}) + C, \qquad i \geq 1, \end{aligned} \tag{3.7}$$

where C is an integral constant, θ also can be expressed by a linear

combination of Legendre polynomials as

$$\theta\big(s(t)\big)=\hat{\theta}(t)=\sum_{i=0}^{\infty}b_iP_i. \tag{3.8}$$

For example, if the curvature is approximated as an nth-order polynomial, it means

$$\kappa\big(s(t)\big)=\hat{\kappa}(t)=\sum_{i=0}^{\infty}a_iP_i, \tag{3.9}$$

where

$$a_i=0, \qquad i\geq n+1. \tag{3.10}$$

Trivially, the series of (3.9) along with the condition (3.10) is uniformly convergent. Thus, by putting the equation (3.9) into (3.6) and integrating the series term-by-term, we have

$$\theta\big(s(t)\big)=\hat{\theta}(t)=\left(\theta_0+\frac{L}{2}\left(a_0-\frac{a_1}{3}\right)\right)P_0+\frac{L}{2}\sum_{i=1}^{\infty}\left(\frac{a_{i-1}}{2i-1}-\frac{a_{i+1}}{2i+3}\right)P_i. \tag{3.11}$$

Then, we can obtain coefficients of the equation (3.8) by comparing it with the equation (3.11):

$$\begin{aligned} b_0&=\theta_0+\frac{L}{2}\left(a_0-\frac{a_1}{3}\right)\\ b_i&=\frac{L}{2}\left(\frac{a_{i-1}}{2i-1}-\frac{a_{i+1}}{2i+3}\right), \qquad i\geq 1. \end{aligned} \tag{3.12}$$

The coefficient a_i of the curvature is calculated by the following steps. First, the equation (2.10) is numerically solved through the simulation and coordinates

of the points that make up the curve of the silicone body are yielded. A matrix X is defined to enumerate the coordinates:

$$X = \begin{bmatrix} x_1 & x_2 & \cdots & x_{n_c} \\ y_1 & y_2 & \cdots & y_{n_c} \end{bmatrix}, \tag{3.13}$$

where n_c is the number of intervals introduced by the numerical integration algorithm. The built-in function *ode45* adopted in this study exploits an adaptive algorithm, so n_c is flexible. The fixation point, $(x_0, y_0) = (0,0)$, is not included the matrix. Next, the angle of a tangent at each interval is numerically calculated from these coordinates and is interpolated to redistribute the points at equal intervals along the curve. These angles compose a vector such that

$$\boldsymbol{\Theta} = \begin{bmatrix} \theta_1 & \theta_2 & \cdots & \theta_{n_d} \end{bmatrix}, \tag{3.14}$$

where n_d is the number of the redivided intervals, and it is set to 40 in this study. n_d can be set arbitrarily as long as it is, for the rational interpolation, lower than the possible minimum of n_c. The vector $\boldsymbol{\Theta}$ can be represented as a sum of discrete Legendre polynomials as follows:

$$\boldsymbol{\Theta} = \sum_{i=0}^{\infty} c_i \boldsymbol{\Pi}_i, \tag{3.15}$$

where $\boldsymbol{\Pi}_i$'s are discretized vectors of the original Legendre polynomials P_i. Their components are determined depending on their dimension n_d, and they still retain

orthogonality that makes it easy to obtain the coefficient c_i by inner product. The discrete equation (3.15) is approximated to the continuous one (3.8) using the following formula:

$$b_i \simeq \frac{c_i}{\nu_i}, \tag{3.16}$$

where ν_i is a normalization factor corresponding to each polynomial vector, and it depends on n_d as well [24]. As the discrete polynomials get closer to the continuous ones, or the dimension n_d of the discrete polynomial vectors increases to infinity, the approximation (3.16) becomes more accurate. At last, the equation (3.12) gives us the coefficients of curvature. Note that we need b_i and c_i for $i = 1$ to $n+1$ to complete the nth-order polynomial (3.9).

3.4. Optimization Formulation

To summarize the design process presented in this thesis, the end-effector coordinates and the body configuration are fitted to a given target by properly setting up cable routing and tension of cable-driven soft actuators. This is formulated as follows:

$$
\begin{aligned}
&\underset{y_1, y_2, y_3, y_4, y_5, \tau}{\text{minimize}} && \lambda_x \left(x_{e,c} - x_{e,t} \right)^2 + \lambda_y \left(y_{e,c} - y_{e,t} \right)^2 + \sum_{i=1}^{n} \lambda_i \left(a_{i,c} - a_{i,t} \right)^2 \\
&\text{subject to} && -r < y_i < r, \qquad i = 1,\ 2,\ 3,\ 4,\ 5 \\
& && \tau_l < \tau < \tau_u,
\end{aligned}
\tag{3.17}
$$

where the subscripts c and t refer to the current design and the target, respectively, λ is a weight assigned according to importance and interest, and the curvature is approximated to an nth-order polynomial. y_i, the coordinates of each control point, constructs the cable routing as explained in the equation (2.12) and is constrained by the radius r of the cylindrical body. Also, the tension τ is constrained to be between the lower bound τ_l and the upper bound τ_u, so that the actuator hardens enough to have a stable configuration with sufficient tension and at the same time it does not undergo an excessive load. The optimization problem is solved with a built-in function *fsolve* of MATLAB.

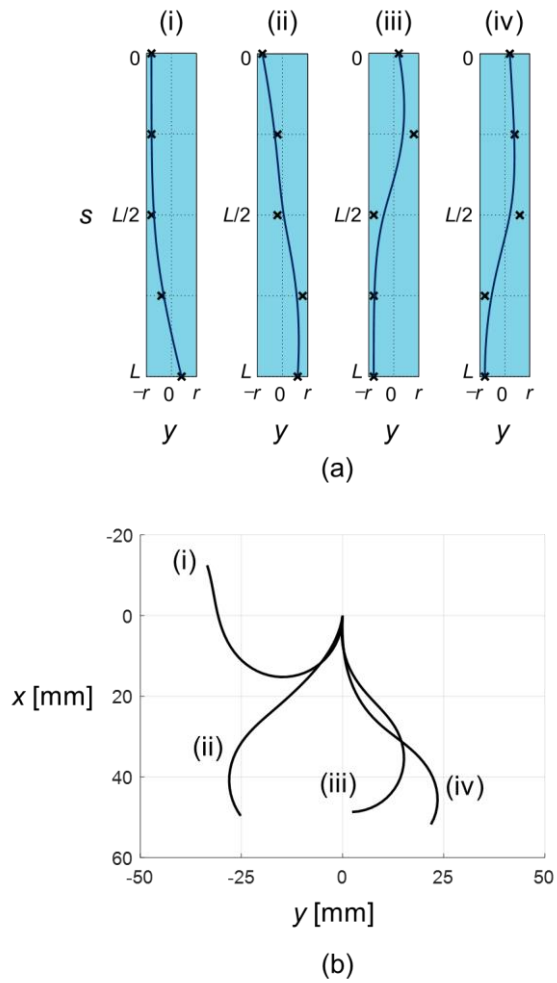

Fig. 3.1. (a) Randomly selected cable routings. (b) Deformation of the actuator resulting from these cable routings. The deformation cannot be perfectly represented with a finite number of degrees of freedom.

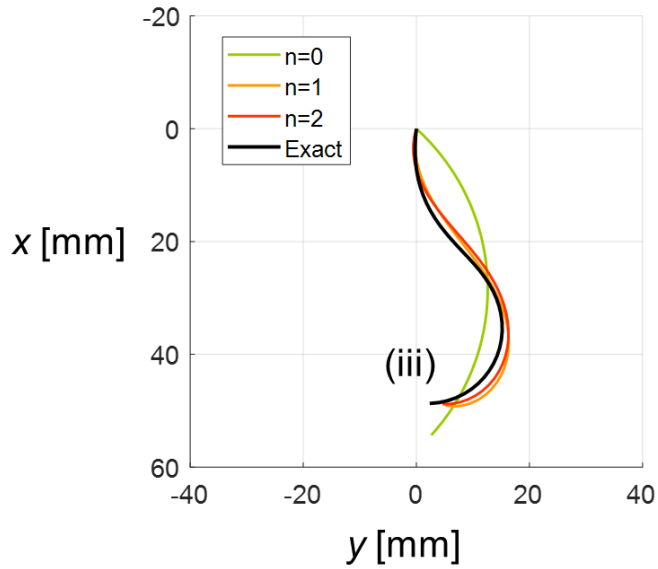

Fig. 3.2. An example of approximating the curvature to nth-order polynomials. It can be seen that the constant curvature does not adequately describe the actuator configuration.

Chapter 4. Feasible Region Inspection

As a conventional robot, a rigid mechanism can drive each degree of freedom independently because motors are attached to each joint. This enables precise and sophisticated operation, but requires a hard and heavy body to support weight of the motors. As a result, robots and humans have been separated for safety. Conversely, soft robots acquire lightness and human-friendliness by placing the driving units outside the body at the cost of giving up the independent actuation of each part. Many researchers in the field of soft robots have studied ways to regain this independence. One of the most representative examples is to make distal parts with softer materials than those used for proximal parts [22], [25]. Actuation on the distal parts is transmitted from the outside of the body to the target area via proximal parts, affecting the proximal parts as well. The differences in stiffness of the parts can mitigate this interference. If only one driving unit operates the entire actuator, the independent actuation of parts is unattainable, as is the case for soft actuators operated by fluid pressure or a single cable. Instead, these actuators can generate distinct deformation at each part by imposing different mechanical constraints on the different parts. The examples include fiber reinforcement of pneumatic soft actuators [11], [12] or the cable routing covered in this study.

However, the distinct deformation of parts is still coupled together. Here comes the problem that it is not clear whether the target shape for design is feasible. Designing with impossible goals would waste a lot of time and effort. To assess the feasibility prior to beginning the design, a kind of guide map can be employed as elucidated below.

4.1. Feasibility Map

In this thesis, both an overall shape of the silicone body and coordinates of the end-effector are explored as a simultaneous target, so proper measures are needed to address the obscure feasibility due to their severe coupling. Since the end-effector coordinates are used as expressive degrees of freedom, one can construct a plane with these coordinates as axes. Then, coefficients of the approximated curvature polynomial are marked at the corresponding points on the plane. This map, with x_e- and y_e-axes, visualizes feasible range and spatial distribution of other expressive degrees of freedom, such as a_0, a_1, $\cdots$. To analyze these maps, it is good to remind that

$$P_i(-1) = \begin{cases} -1, & \text{if } i \text{ is odd} \\ 1, & \text{if } i \text{ is even} \end{cases} \qquad (4.1)$$
$$P_i(1) = 1,$$

which means that the larger the value of a_i becomes, the more the actuator bends clockwise at the distal end, regardless of i. At the proximal end, on the other hand, the bending orientation depends on i.

The maps are drawn based on simulation results. With cable routing and tension as an input, the corresponding output—a matrix X that contains coordinates of the points forming the silicone body—is obtained through a simulation. Then the last point of X is chosen as the end-effector, a_i's are calculated as described in Section 3.3, and they are marked at the end-effector coordinates. In this way, one simulation performed with a certain set of input values results in one point on the map. This marking process is repeated for a large number of input values covering all possible cases. In this thesis, nine values $y_i = -0.8r,\ -0.6r,\ -0.4r,\ \cdots,\ 0.8r$ for the coordinates of control points and 21 values $\tau = \tau_l,\ \tau_l + \Delta\tau,\ \tau_l + 2\Delta\tau,\ \cdots,\ \tau_u$ with $\Delta\tau = (\tau_u - \tau_l)/20$ for the tension were assigned. Excepting symmetric cable routings in order to save time, 620025 simulations were performed. The total time spent to generate the data was approximately 8.5 hours.

Drawing these maps can be thought to be a very time-consuming task. However, this is worth the time because the maps can be generally applied to planar cable-driven soft actuators. It is inferred that even if some dimensions,

mechanical properties, or necessary tension of the soft actuators changes, the main modes of deformation and their spatial distribution would not change abruptly. Understanding tendency of the maps with respect to those variable factors, specifications of an actuator to be designed can be conversely determined from the maps according to the design target.

4.2. Map Analysis

The maps visualize various properties of the actuator depending on how the data is represented. The simplest type of map is shown in Fig. 4.1. In the figure, there is a grid spaced at 1mm apart on the plane, and the color of each square represents the number of simulations where the end-effector positions within the square. That is, this figure depicts the whole area that the actuator can reach by having a proper cable routing. The dark color of a square means that the actuator can reach the square with various configurations. Note that only points with positive y_e-coordinates are plotted in the figure. Points with negative y_e-coordinates will exhibit symmetric distribution by the symmetric cable routing.

Another type of map that focuses on the coefficient a_0, the mean curvature, is presented in Fig. 4.2. The figure has a similar grid and the color in Fig. 4.2 (a), (b), and (c) refers to the 10th percentile, the 90th percentile, and their differences,

respectively, all of which are useful information to figure out distribution of a_0. Generally, absolute values of the mean curvature increases as the end-effector goes higher towards the base, which is consistent with intuition. It is also remarkable that, as indicated by a dashed line in Fig. 4.2 (c), there exists an area where the gap between two percentiles is particularly large. This implies that there is more than one mode of configuration. These modes will be identified below. A map that is similar to Fig. 4.2 but focuses on a_1 is shown in Fig. 4.3. From the figure, it can be seen that distance to the fixation point rather than height of the end-effector is the main factor in determining distribution of a_1. In other words, a large absolute value of a_1 suggests that the actuator deforms to shrivel. The overlapping areas of different modes are broader in Fig. 4.3 (c) than in the previous one.

The final type of map in Fig. 4.4 describes distribution of characteristic configurations selected by a certain combination of the coefficients. This map consists of several pieces, each of which covers one of the characteristic configurations. In the figure, a_0 and a_1 are divided into four and three sections, respectively, and the total twelve characteristic configurations are shown with their distribution. This type of map directly assists in determining feasibility. One may set target position of the end-effector first, and then consider possible configurations referring to this map, and vice versa. The aforementioned areas

where a couple of configuration modes appear also can be seen in the figure.

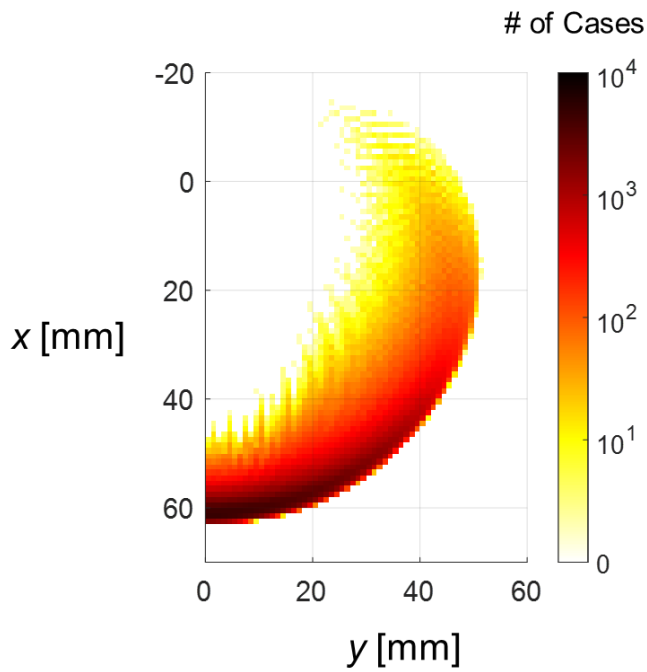

Fig. 4.1. A reachable area of the actuator by having a proper cable routing. A grid is spaced at 1mm apart and colored according to the number of simulations where the end-effector positions within each square.

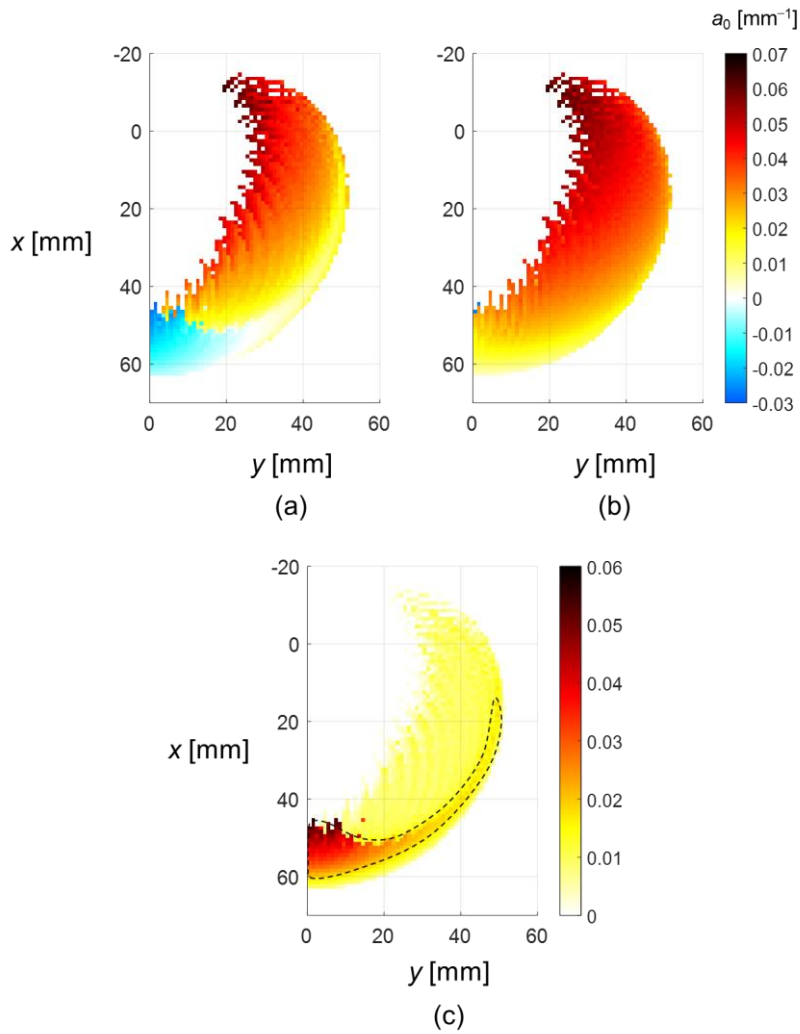

Fig. 4.2. Distribution of a_0. (a) The 10th percentile. (b) The 90th percentile. (c) Their differences. The primary factor affecting the distribution is height of the end-effector. In the area marked by the dashed line, the large difference between the two percentiles implies that there is more than one mode of configuration.

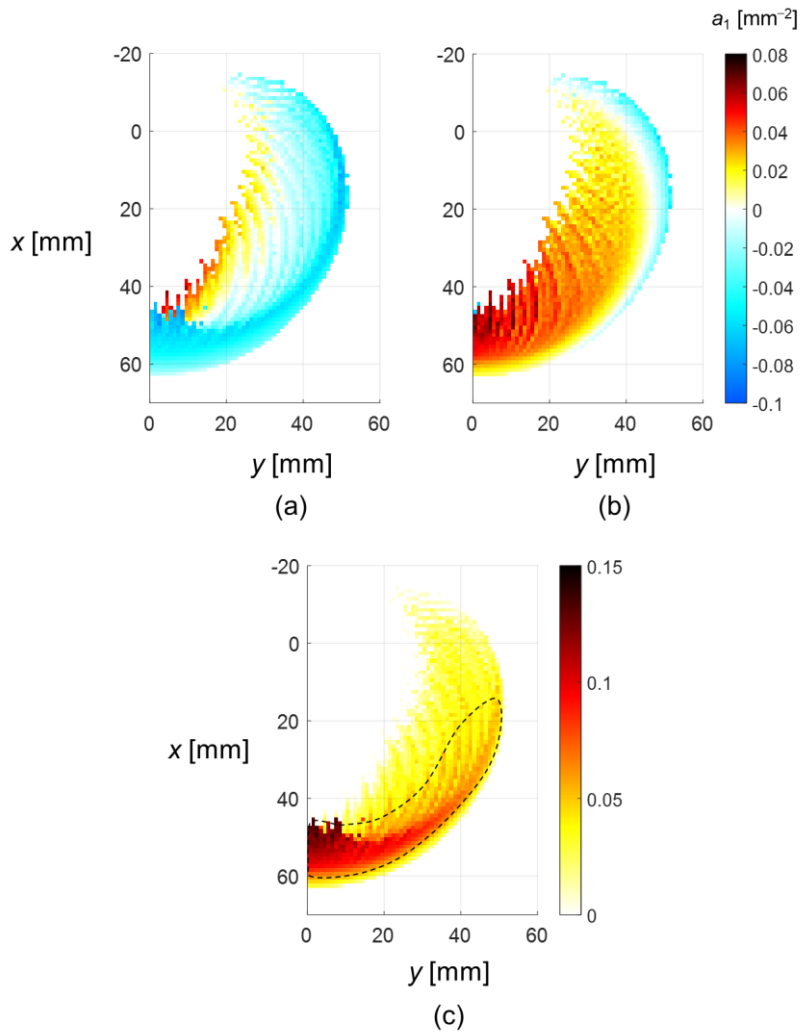

Fig. 4.3. Distribution of a_1. (a) The 10th percentile. (b) The 90th percentile. (c) Their differences. The primary factor affecting the distribution is distance between the fixation point and the end-effector. The area where more than one configuration mode exists is broader than that in Fig. 4.2 (c).

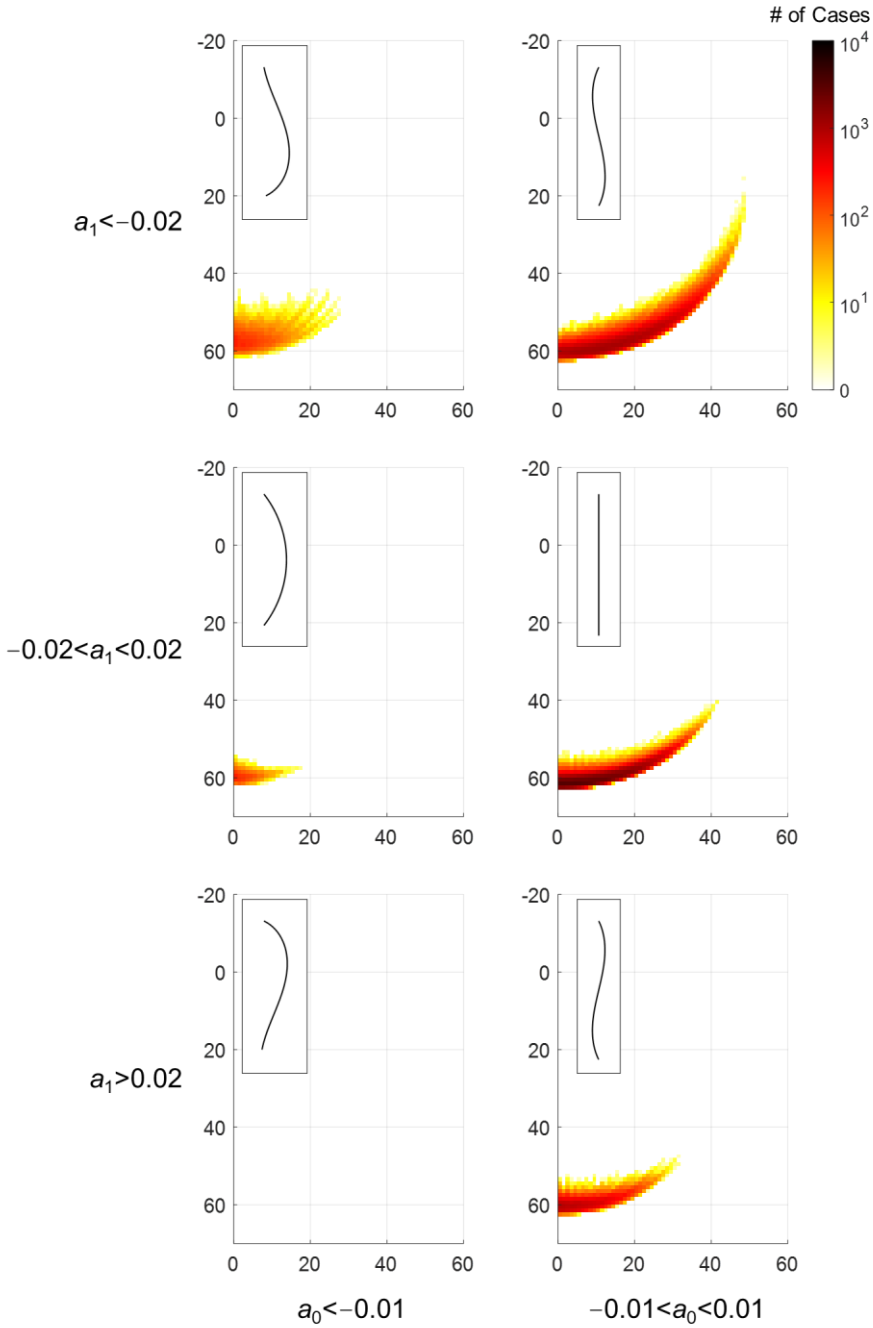

Fig. 4.4. Distribution of twelve characteristic configurations classified according to the range of coefficients. The pieces of the map show where a certain configuration occur.

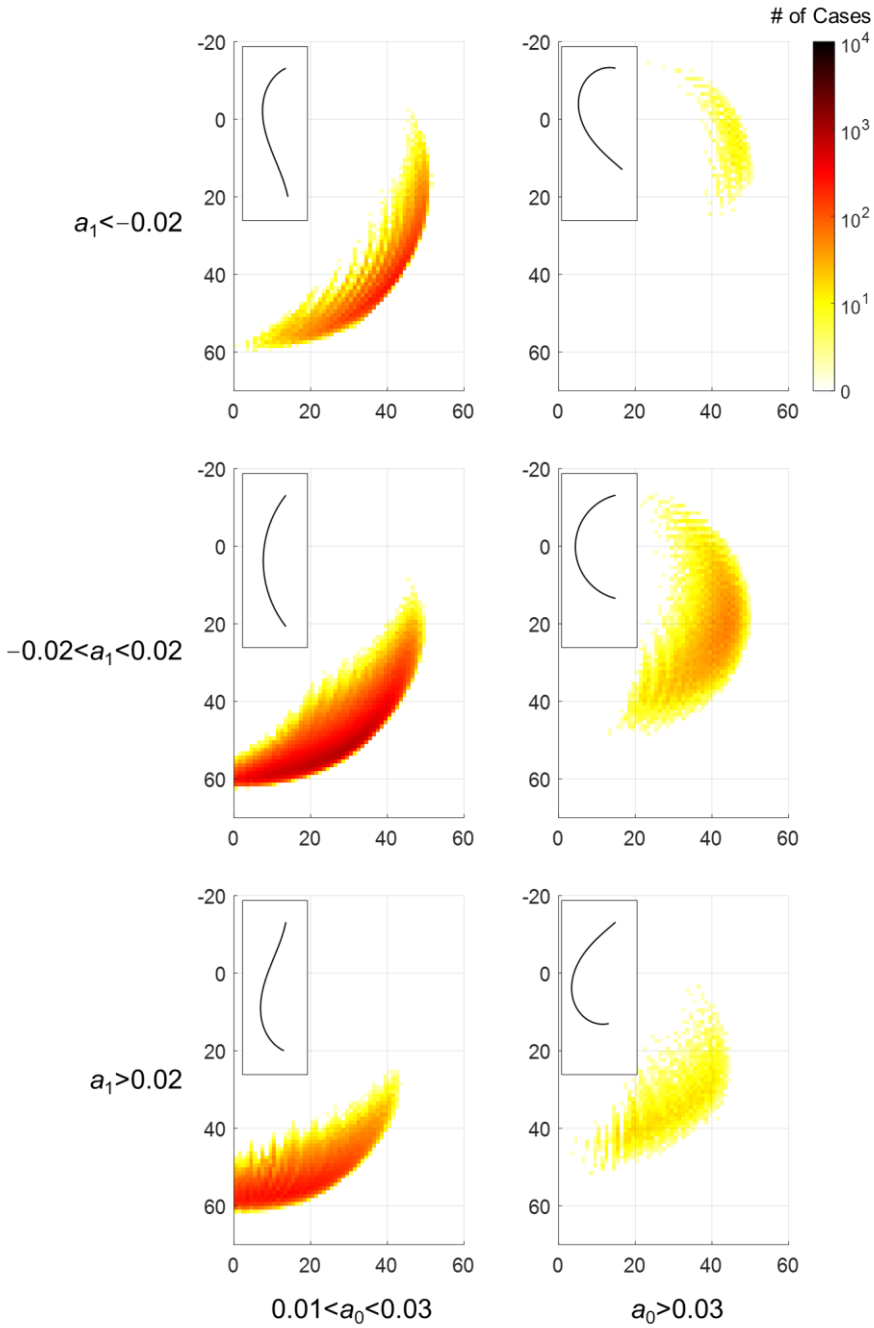

Fig. 4.4. *(continued.)*

Chapter 5. Validation

In this chapter, it is demonstrated that the optimization problem and the design process proposed in this thesis so far work well in practice. For this purpose, the actual actuator was fabricated, cable routing of which was optimized to match the target. Next, an experimental setup that can apply desired tension to a cable was devised and the experimental results were compared with those of simulations. Finally, it is confirmed that the newly designed actuators deform to satisfy the target with high accuracy, which proves the validity of this thesis.

5.1. Cable Routing Optimization

To determine a cable routing of the actuator to be designed, the optimization problem (3.17) is solved. In this study, the length L and the radius r of the actuator is set to 65mm and 5mm, respectively. The curvature is approximated up to a second-order polynomial and the weights are empirically set as $\lambda_x = \lambda_y = 1$, $\lambda_0 = 100$, $\lambda_1 = 50$, and $\lambda_2 = 25$. Target values and optimized results are listed in Table 5.1. The optimized results in the table was obtained by simulations with the optimized cable routings presented in Fig. 5.1 and the optimized tension of 1.95N

2.00N for each case. Before starting the design with the target values, we can take the map in Fig. 4.4 to assure that the problem has a plausible answer. Most of the errors in the end-effector coordinates and the curvature coefficients are below 5%, which verifies the efficacy of the proposed design process. The errors more than 10% are also tolerable, considering the adaptability of soft robots. It is possible to reduce an error of a certain expressive degree of freedom by controlling the corresponding weights in the equation (3.17).

5.2. Fabrication

The cylindrical silicone body is made from Dragon Skin 10 Medium (Smooth-on, Inc.), which is manageable and human-friendly. Its softness also alleviates requirements for cables and motors. A kink-free cable is used as a tension transmitter because it returns to its original straight shape even after severe deformation. The fabrication is done through a combination of the lamination-based method and the retractable-pin-based method [26]. Molds to cast silicone body are printed with a 3D printer Objet Connex 260 and a photosensitive polymer Vero White (Stratasys, Ltd.). The mold in Fig. 5.2 (a) represents the one used for the first casting, where only half the silicone body is cast. Since the inner surface of the mold has a protrusion along the cable routing, the semi-cylindrical silicone

body is grooved along it. A PTFE tube is inserted into this groove and the assembled silicone body is mounted on another mold shown in Fig. 5.2 (b) for the second casting. The tube plays a role of a retractable pin—it takes up space and prevents liquid silicone from flowing in while curing, so that there remains an empty channel after the tube is retracted from the cured silicone. The essential difference between the PTFE tube and a pin is that the tube is flexible and therefore can bend. In this way, a cylindrical silicone body with a curved channel can be made. The diameter of the channel, i.e. the outer diameter of the PTFE tube, is 1mm, which is small enough to neglect in simulations.

5.3. Experiment

Experiments are conducted to confirm that the cable-driven soft actuator designed through the optimization works well in practice. To this end, an experimental device is installed at the edge of a table as can be seen in Fig. 5.3. First, a 3D-printed basket is screwed to the table and the fabricated actuator is clamped vertically at the basket's sticking part out of the table. The cable is connected to a load cell and a linear motor via a pulley. The models of the load cell, 333FB (KTOYO Co., Ltd.), and the motor, L16-R Linear Servo (Actuonix Motion Devices, Inc.) are such that they are suitable for the tension ranging up to 2N, which is

required for this study. Both the load cell and the motor are connected to the Arduino Uno and controlled by a simple feedback algorithm to apply desired tension to the cable. Increasing the tension in several steps, the configuration of the silicone body can be measured by a grid behind it. Coordinates of the points on a centerline of the silicone body are recorded and compared with the simulation in Fig. 5.4. We can see in the figure that the deformation of the actuator is almost identical in simulations and experiments. In conclusion, the design and fabrication procedures presented in this thesis produce valid results.

Table 5.1. Target values and simulation results using optimized cable routings and tension

	x_e **[mm]**	y_e **[mm]**	a_0 **[mm^{-1}]**	a_1 **[mm^{-2}]**	a_2 **[mm^{-3}]**
Target I	50.00	5.000	-0.0250	-0.0600	0.0150
Optimized	49.99	4.998	-0.0244	-0.0599	0.0131
Error	-0.02%	-0.04%	2.40%	0.17%	-12.7%
Target II	10.00	50.00	0.0150	-0.0700	-0.0300
Optimized	10.02	49.94	0.0169	-0.0713	-0.0287
Error	0.02%	-0.12%	12.7%	-1.86%	4.33%

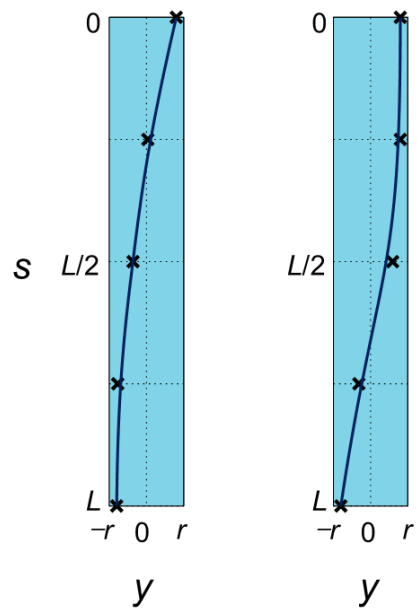

Fig. 5.1. Cable routings optimized with arbitrary target values in Table 5.1.

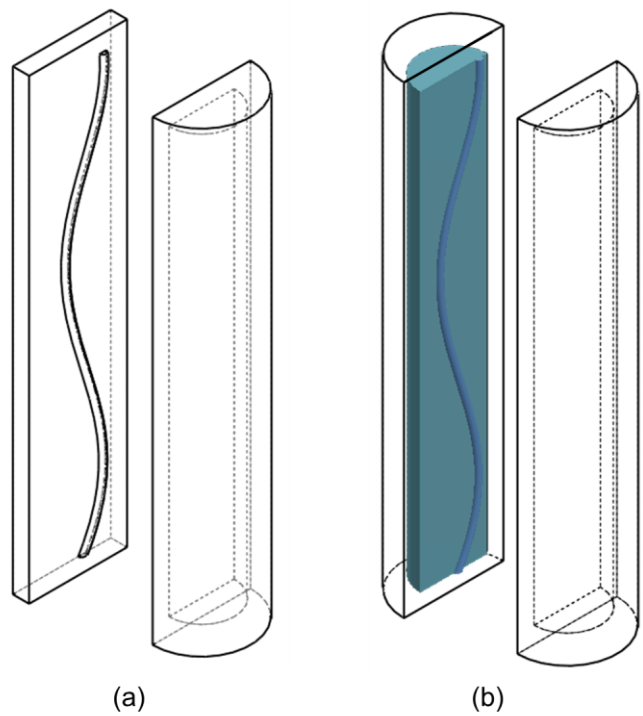

Fig. 5.2. (a) Mold for the first casting. (b) Mold for the second casting. By the first casting, half of the silicone body with a curved groove is cast. By the second casting, the other half is attached to the semi-cylindrical silicone body with a PTFE tube inserted into the groove. Pulling the tube away after curing completes the fabrication.

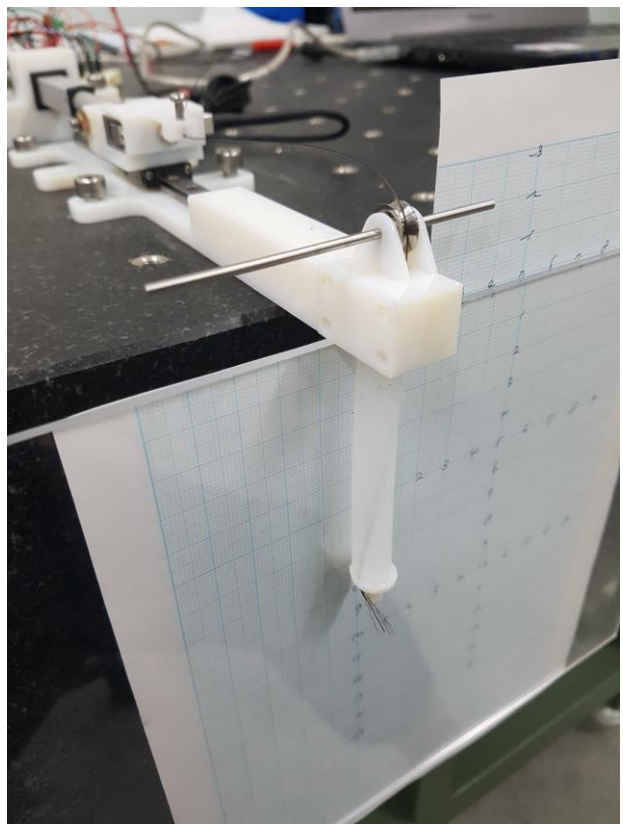

Fig. 5.3. Experimental setup including a load cell, a linear motor, and an Arduino. The actuator is clamped vertically and the configuration of the silicone body can be measured by a grid behind the actuator.

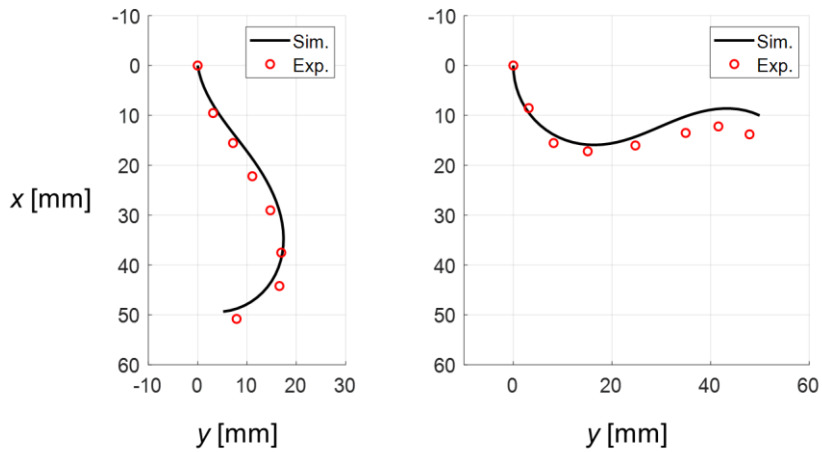

Fig. 5.4. Results of the experiments conducted with the fabricated actuators that have the optimized cable routings. Little discrepancy implies the validity of this study.

Chapter 6. Conclusion

Soft robots, unlike conventional rigid robots, are made of materials that are similar in stiffness to biological tissue. This softness enables safe and flexible operation close to people or in an unorganized environment. However, it also increases the complexity of their design and thus impedes their utilization. In this thesis, an systematic design process with minimal human intervention was proposed. What was designed in this study is the cable routing of planar cable-driven soft actuators. Their actuation was modeled by coupling the Cosserat model for the silicone body and the cable, and the cable routing was constructed as a B-spline with five control points. The material moduli for mechanical properties were fitted to the experimental results to reduce uncertainty. Then, for optimization formulation, an appropriate expression that can represent curved configurations of the silicone body was newly proposed. The expression using Legendre polynomials has several merits, one of which is that dependency between the expressive degrees of freedom can be visualized as a map. This is especially important because the actuator has a single driving unit outside its body. The different types of maps provide an overview of how the expressive degrees of freedom are coupled. Actual fabrication and experiments were performed according to the design flows

proposed in this thesis, and the results demonstrated the validity of this study.

This thesis also leaves future works to advance the research. In this study, a very simplified model was adopted that excludes friction or hysteresis for ease of computation. More sophisticated models involving those are needed to make the design more accurate and realistic. Cosserat models that take account of real-time dynamics [27] or FEM models that include Lagrangian multipliers [28] are expected to make further advances. In this thesis, only planar routings are dealt with due to the difficulty of fabrication, but if spatial channels in silicone body can be fabricated by 3D printing [9], [10], [13] or other methods, it would be possible to design a wider variety of configurations and movements of the actuators. By increasing the number of cables to more than one, target performances other than a single stationary configuration can be set: the transitional process of change in the configuration or the trajectory of the end-effector, for example.

This thesis contributes to the design automation indispensable for commercialization of soft robots. This study can be directly applied to design fingers of a gripper or legs of a locomotive robot. Also, this study can facilitate the design of personalized equipment, such as wearable devices, that requires customized design for each use. I envision that advanced research on the design automation of soft robots will bring them closer to us in near future.

References

[1] C. Majidi, “Soft robotics: A perspective—Current trends and prospects for the future,” *Soft Robot.*, vol. 1, no. 1, pp. 5-11, Mar. 2014.

[2] D. Rus and M. T. Tolley, “Design, fabrication and control of soft robots,” *Nature*, vol. 521, pp. 467-475, May 2015.

[3] M. Cianchetti, C. Laschi, A. Menciassi, and P. Dario, “Biomedical applications of soft robotics,” *Nat. Rev. Mater.*, vol. 3, pp. 143-153, Jun. 2018.

[4] H. Lipson, “Challenges and opportunities for design, simulation, and fabrication of soft robots,” *Soft Robot.*, vol. 1, no. 1, pp. 21-27, Mar. 2014.

[5] H. Lin, G. G. Leisk, and B. Trimmer, “GoQBot: A caterpillar-inspired soft-bodied rolling robot,” *Bioinspir. Biomim.*, vol. 6, no. 2, Apr. 2011.

[6] C. Laschi, M. Cianchetti, B. Mazzolai, L. Margheri, M. Follador, and P. Dario, “Soft robot arm inspired by the octopus,” *Adv. Robot.*, vol. 26, no. 7, pp. 709-727, Apr. 2012.

[7] S. Seok, C. D. Onal, K.-J. Cho, R. J. Wood, D. Rus, and S. Kim, “Meshworm: A peristaltic soft robot with antagonistic nickel titanium coil actuators,” *IEEE/ASME Trans. Mechatron.*, vol. 18, no. 5, pp. 1485-1497, Jul. 2012.

[8] A. Seibel and L. Schiller, “Systematic engineering design helps creating new soft machines,” *Robot. Biomim.*, vol. 5, no. 5, Oct. 2018.

[9] J. Hiller and H. Lipson, “Automatic design and manufacture of soft robots,” *IEEE Trans. Robot.*, vol. 28, no. 2, pp. 457-466, Apr. 2012.

[10] L. Ma, Y. Zhang, Y. Liu, K. Zhou, and X. Tong, “Computational design and

fabrication of soft pneumatic objects with desired deformations," *ACM Trans. Graph.*, vol. 36, no. 6, Nov. 2017.

[11] F. Connolly, C. J. Walsh, and K. Bertoldi, "Automatic design of fiber-reinforced soft actuators for trajectory matching," *Proc. Natl. Acad. Sci. U. S. A.*, vol. 115, no. 1, pp. 51-56, Jan. 2017.

[12] G. Singh and G. Krishnan, "Designing fiber-reinforced soft actuators for planar curvilinear shape matching," *Soft Robot.*, vol. 7, no. 1, pp. 109-121, Feb. 2020.

[13] M. Schaffner, J. A. Faber, L. Pianegonda, P. A. Rühs, F. Coulter, and A. R. Studart, "3D printing of robotic soft actuators with programmable bioinspired architectures," *Nat. Commun.*, vol. 9, Feb. 2018.

[14] K. Oliver-Butler, J. Till, and C. Rucker, "Continuum robot stiffness under external loads and prescribed tendon displacements," *IEEE Trans. Robot.*, vol. 35, no. 2, pp. 403-419, Apr. 2019.

[15] T. Umedachi, V. Vikas, and B. A. Trimmer, "Softworms: The design and control of non-pneumatic, 3D-printed, deformable robots," *Bioinspir. Biomim.*, vol. 11, no. 2, Mar. 2016.

[16] J. Starke, E. Amanov, M. T. Chikhaoui, and J. Burgner-Kahrs, "On the merits of helical tendon routing in continuum robots," in *Proc. IEEE/RSJ Int. Conf. Intell. Robots Syst.*, 2017, pp. 6470-6476.

[17] J. C. Case, E. L. White, V. SunSprial, and R. Kramer-Bottiglio, "Reducing actuator requirements in continuum robots through optimized cable routing," *Soft Robot.*, vol. 5, no. 1, pp. 109-118, Feb. 2018.

[18] J. Barreios, K. W. O'Brien, S. Hong, M. F. Xiao, H.-J. Yang, and R. F.

Shepherd, “Configurable tendon routing in a 3D-printed soft actuator for improved locomotion in a multi-legged robot,” in *Proc. IEEE Int. Conf. Soft Robot.*, 2019, pp. 94-101.

[19] D. C. Rucker and R. J. Webster III, “Statics and dynamics of continuum robots with general tendon routing and external loading,” *IEEE Trans. Robot.*, vol. 27, no. 6, pp. 1033-1044, Dec. 2011.

[20] F. Renda, M. Giorelli, M. Calisti, M. Cianchetti, and C. Laschi, “Dynamic model of a multibending soft robot arm driven by cables,” *IEEE Trans. Robot.*, vol. 30, no. 5, pp. 1109-1122, Oct. 2014.

[21] R. J. Webster III and B. A. Jones, “Design and kinematic modeling of constant curvature continuum robots: A review,” *Int. J. Robot. Res.*, vol. 29, no. 13, pp. 1661-1683, Nov. 2010.

[22] C. Bergeles, A. H. Gosline, N. V. Vasilyev, P. J. Codd, P. J. del Nido, and P. E. Dupont, “Concentric tube robot design and optimization based on task and anatomical constraints,” *IEEE Trans. Robot.*, vol. 31, no. 1, pp. 67-84, Feb. 2015.

[23] R. Roy, L. Wang, and N. Simaan, “Modeling and estimation of friction, extension, and coupling effects in multisegment continuum robots,” *IEEE/ASME Trans. Mechatron.*, vol. 22, no. 2, pp. 909-920, Apr. 2017.

[24] M. F. Aburdene, “On the computation of discrete Legendre polynomial coefficients,” *Multidim. Syst. Sign. P.*, vol. 4, pp. 181-186, Apr. 1993.

[25] M. Li, R. Kang, S. Geng, and E. Guglielmino, “Design and control of a tendon-driven continuum robot,” *T. I. Meas. Control.*, vol. 40, no. 11, pp.

3263-3272, Jul. 2018.

[26] A. D. Marchese, R. K. Katzschmann, and D. Rus, “A recipe for soft fluidic elastomer robots,” *Soft Robot.*, vol. 2, no. 1, pp. 7-24, Mar. 2015.

[27] J. Till, V. Aloi, and C. Rucker, “Real-time dynamics of soft and continuum robots based on Cosserat rod models,” *Int. J. Robot. Res.*, vol. 38, no. 6, pp. 723-746, May 2019.

[28] E. Coevoet, T. Morales-Bieze, F. Largilliere, Z. Zhang, M. Thieffry, M. Sanz-Lopez, B. Carrez, D. Marchal, O. Goury, J. Dequidt, and C. Duriez, “Software toolkit for modeling, simulation, and control of soft robots,” *Adv. Robot.*, vol. 31, no. 22, pp. 1208-1224, Nov. 2017.

초 록

소프트로봇은 전통적인 강체 로봇과 비교되지 않는 적응성과 안정성 등의 장점을 가진 덕분에 최근 상당한 관심을 끌고 있다. 그러나 이에 수반되는 복잡성은 소프트로봇이 기대만큼 널리 사용되지 못하는 원인이 되고 있다. 특히, 소프트로봇의 설계는 연구자의 많은 경험과 시간을 필요로 해왔다. 이 연구에서는 한층 체계적인 방식으로 케이블 구동식 평면 소프트 액추에이터를 설계한다. 이를 위해, 우선 르장드르 다항식을 사용하여 연속적으로 곡률이 변하는 소프트 액추에이터의 곡선 형태를 표현하였다. 이 표현 방법은 설계 문제의 정식화에 필요한 설계 변수의 개수를 최소화하면서 이들의 물리적 의미를 보존한다. 더불어 이렇게 선택된 설계 변수는 서로에 대한 의존성을 시각화할 수 있는 일종의 지도를 그리는 데에 적합하다. 이러한 지도를 통해 우리는 본격적으로 설계를 시작하기 전에 설계 문제가 실제로 답을 가지고 있는지 미리 확인할 수 있다. 이 논문에서 새롭게 제안된 최적화 기반의 설계 절차는 임의로 선택된 목표치에 대하여 검증되었다. 또한 실제 실험을 수행하여 이 설계 절차로 얻어진 설계안이 현실에서도 유효함을 확인할 수 있었다.

주요어: 최적화 기반 설계, 케이블 구동식 액추에이터, 소프트로봇, 설계 가능성

학 번: 2018-24324